Earth and Planetary Science Letters 310 (2011) 1–8

Contents lists available at ScienceDirect

Earth and Planetary Science Letters

journal homepage: www.elsevier.com/locate/epsl

The size-frequency distribution of elliptical impact craters

G.S. Collins [a,*], D. Elbeshausen [b], T.M. Davison [a], S.J. Robbins [c], B.M. Hynek [c]

[a] Department of Earth Science and Engineering, Imperial College, London, UK
[b] Museum für Naturkunde, Leibniz-Institute at the Humboldt-University of Berlin, Germany
[c] Laboratory for Atmospheric and Space Physics, University of Colorado at Boulder, USA

ARTICLE INFO

Article history:
Received 5 January 2011
Received in revised form 7 June 2011
Accepted 22 July 2011
Available online 27 August 2011

Editor: T. Spohn

Keywords:
impact craters
oblique impact
elliptical crater
numerical modeling

ABSTRACT

Impact craters are elliptical in planform if the impactor's trajectory is below a threshold angle of incidence. Laboratory experiments and 3D numerical simulations demonstrate that this threshold angle decreases as the ratio of crater size to impactor size increases. According to impact cratering scaling laws, this implies that elliptical craters occur at steeper impact angles as crater size or target strength increases. Using a standard size-frequency distribution for asteroids impacting the terrestrial planets we estimate the fraction of elliptical craters as a function of crater size on the Moon, Mars, Earth, Venus and Mercury. In general, the expected fraction of elliptical craters is ~2–4% for craters between 5 and 100-km in diameter, consistent with the observed population of elliptical craters on Mars. At larger crater sizes both our model and observations suggest a dramatic increase in the fraction of elliptical craters with increasing crater diameter. The observed fraction of elliptical craters larger than 100-km diameter is significantly greater than our model predictions, which may suggest that there is an additional source of large elliptical craters other than oblique impact.

1. Introduction

Impact craters are the dominant landform on nearly every solid planetary surface in the solar system. While the vast majority of these craters are very nearly circular in planform, a few percent of craters show pronounced elongation of the crater in one direction (Bottke et al., 2000; Melosh, 1989; Schultz and Lutz-Garihan, 1982).

The dominant cause of crater ellipticity is oblique impact; impact craters are elliptical if the impactors trajectory is below a threshold angle of incidence (Gault and Wedekind, 1978). Astrodynamical arguments demonstrate that oblique impacts are common; the most probable impact angle is 45° to the target plane and half of all impacts occur at a shallower angle of incidence (Gilbert, 1893; Shoemaker, 1962). The relatively few elliptical craters on planetary surfaces suggests that only impacts at angles less than ~12° produce elliptical craters (Bottke et al., 2000).

The paucity of elliptical impact craters on planetary surfaces is so apparent that circularity is often used as supporting (non-diagnostic) evidence for the impact origin of putative terrestrial impact structures (French and Koeberl, 2010). However, elliptical craters are an important fraction of any crater population and recent measurements of the largest impact basins in the Solar System, including the South Pole-Aitkin basin on the moon, Caloris basin on Mercury, and the putative Borealis impact basin on Mars, suggests a propensity for elliptical crater formation in giant impacts (Andrews-Hanna and Zuber, 2010). Hence, contrary to popular belief, impact may be more likely to produce an elliptical crater than a circular one, in some regimes.

A key question in predicting impact crater populations is: what controls the elliptical crater threshold angle? The effect of impact angle on crater ellipticity (and other measures of crater asymmetry) has been investigated directly by experiments (Anderson et al., 2004; Burchell and Mackay, 1998; Christiansen et al., 1993; Gault and Wedekind, 1978) and numerical impact simulations (this work; Davison et al., in press; Elbeshausen and Wünnemann, 2010), as well as indirectly by remote sensing (Bottke et al., 2000; Herrick and Forsberg-Taylor, 2003; Schultz and Lutz-Garihan, 1982). However, complete understanding of the conditions under which elliptical craters are formed is lacking. In this paper, we use evidence from new numerical simulations and laboratory experiments to develop a new scaling law for elliptical crater formation and use this to make testable predictions of elliptical crater populations on planetary surfaces.

2. Elliptical crater threshold angle

The elliptical crater threshold angle, θ_e, is commonly defined as the impact angle required to form a crater of ellipticity (length/width) $e = 1.1$ or 1.2 (Bottke et al., 2000). Laboratory-scale impact experiments (Burchell and Mackay, 1998; Christiansen et al., 1993; Gault and Wedekind, 1978) have demonstrated that θ_e depends on the target material and the projectile-target density ratio. Craters formed in strong, ductile metallic targets and strong, brittle rock targets tend to be elliptical for impact angles up to 30–40°, whereas craters formed in sand are only elliptical in highly oblique impacts ($\theta < 5°$). This

* Corresponding author at: Department of Earth Science and Engineering, Imperial College, London, SW7 2BP, UK. Tel.: +44 20 75941518; fax: +44 20 75947444.
E-mail address: g.collins@imperial.ac.uk (G.S. Collins).

0012-821X/$ – see front matter © 2011 Elsevier B.V. All rights reserved.
doi:10.1016/j.epsl.2011.07.023

suggests that material strength has an important influence on θ_e (Bottke et al., 2000; Gault and Wedekind, 1978); however, it is not clear which experimentally-determined value of θ_e is the most appropriate for planetary-scale cratering. $\theta_e = 30°$ would imply a 25% probability of elliptical crater formation; whereas, $\theta_e = 5°$ would imply a <1% probability of elliptical crater formation.

Small-scale crater formation in cohesionless materials, such as sand, is different to small-scale crater formation in materials with substantial cohesive strength, such as metal or rock (Holsapple, 1993). In the case of sand, crater growth is controlled by the competition between inertial versus gravitational and frictional stresses. Crater growth is retarded by the weight of the displaced target material and the frictional resistance between sand grains, both of which are greater under higher gravity. Consequently, such impacts are termed gravity-controlled (or gravity regime) impacts and are most usefully quantified by an inverse Froude number gL/v^2 (g is gravity, L is impactor diameter, v is impact velocity). In the contrasting case of materials with high cohesion, crater growth is controlled by the competition between inertial stresses and the target's cohesive strength. Hence, these impacts are termed strength-controlled (or strength regime) impacts and are most usefully quantified by the ratio $Y/\rho v^2$ (ρ and Y are the density and cohesive strength of the target, respectively). In general, the relative influence of gravity and strength can be measured by the ratio $S = Y/\rho gL$. Large values of S imply strength-dominated cratering; small values imply gravity dominated cratering. An intermediate regime exists, which spans the range $0.1 \lesssim S \lesssim 10$, where both gravity and strength act to retard crater growth (Holsapple and Schmidt, 1979). The characteristic value of Y for a planetary surface is not well understood, but is thought to be on the order of 1 MPa (Melosh, 1977, 1989), in which case all impacts on Mars (for example) with an impactor diameter smaller than 10 m are dominated by strength whereas all impacts with an impactor diameter greater than 1 km are dominated by gravity. Hence, laboratory impacts in sand would appear to be the best analog for large-scale planetary impacts, but this would imply <1% probability of elliptical crater formation.

Bottke et al. (2000) proposed a simple conceptual model to reconcile the observed number of elliptical craters on the terrestrial planets with the results of impact experiments. They noted that the experimentally-determined elliptical crater threshold angle depends on the ratio of crater diameter to impactor diameter. Using crater scaling laws, they suggested that the appropriate threshold angle for planetary surfaces should be ~12°, intermediate between the experimental values for sand and metal, and consistent with the observed number of elliptical craters. A prediction of this model is that the elliptical crater threshold angle should increase with impactor size in gravity-dominated cratering (Bottke et al., 2000).

In this work we used three-dimensional numerical impact simulations to quantify the individual effect of each impactor or target property on θ_e. For several different permutations of impactor size, impact velocity, target strength and gravity, we used the iSALE-3D shock physics code (Amsden and Ruppel, 1981; Elbeshausen et al., 2009) to simulate crater formation for a range of different impact angles between 10 and 90° to the target plane (typically every 5–10°). In all simulations the target and impactor density were the same. The Tillotson equation of state, with parameters for aluminum or granite (Melosh, 1989), was used to model the thermodynamic response of the impactor and target material, but the choice of equation of state did not influence our results. Impact velocity was varied between 5 km/s and 20 km/s; however, to limit computational expense, and to allow future experiments to verify our results, most simulations assumed a relatively slow impact velocity of 5–8 km/s (c.f. Table 2). Target (and impactor) strength was modeled using a simple Drucker-Prager strength model (see Elbeshausen et al., 2009, for details), where the shear strength $Y = Y_0 + kp$ and Y_0 and k are material constants (the cohesion and coefficient of internal friction, respectively) and p is pressure. Y_0 and k were chosen to span a large parameter space that encompassed values typical for experimental targets, both ductile (high Y_0, low k) and brittle (high Y_0, high k) and values considered representative of planetary surfaces at both small scale (low Y_0, high k) and large scale (low Y_0, low k). Importantly, the range of target properties investigated implies that our results span all cratering regimes, from strength-dominated to gravity-dominated cratering.

For each suite of simulation results we calculated the final crater planform, as measured at the ambient surface. From the length (along-range diameter) and width (across-range diameter) of the crater (at the pre-impact surface) we calculated the crater ellipticity at each impact angle and used these data to estimate θ_e, the impact angle below which the crater planform displayed an ellipticity greater than 1.1. This typically required a linear interpolation between two data-points of crater ellipticity versus impact angle that bridged the critical ellipticity of 1.1. The error in estimating the ellipticity angle in this way is approximately $\pm 2.5°$. Further details of our modeling approach (including resolution studies and comparison between numerical results and laboratory experiments) are described in Elbeshausen et al. (2009) and Davison et al. (in press).

Our numerical simulation results, together with the results of laboratory experiments, show that θ_e is a function of impactor size, impact velocity and target strength (Table 1). The threshold angle increases with increasing target strength (in particular, cohesion), impactor size and gravity, and with decreasing impact velocity. The data in Table 1 are synthesized most usefully by considering the elliptical crater threshold angle as a function of crater diameter divided by impactor diameter D/L for each suite of experiments (Bottke et al., 2000). However, D/L is a measure of cratering efficiency, which is itself a function of impact angle; hence, we quantify the cratering efficiency for a suite of experiments where the impact angle varies by the ratio of crater diameter to impactor diameter for a fixed impact angle, taken to be vertical, $D_\perp/L$. Note that $D_\perp$ as used to define the cratering efficiencies in Table 1 is the diameter of the final crater as measured at the pre-impact surface (i.e., the apparent crater diameter). However, as no significant late-stage collapse of the crater occurred in any of the experiments or models, the results are also representative of the apparent transient (pre-collapse) crater diameter. Indeed, as extensive transient crater collapse is an important feature of large-scale crater formation, in the following analysis we assume $D_\perp/L$ is a measure of the cratering efficiency of the transient crater, rather than of the final crater, when applying our results to large complex impact craters.

Fig. 1 shows that θ_e follows a single trend when plotted against $D_\perp/L$, regardless of the target material, impactor size or gravity. The trend also appears to be independent of impact velocity; however, as only one suite of simulations used an impact velocity greater than 10 km/s, additional high-velocity simulations are required to verify this. The trend is fit well by the expression:

$$\theta_e = 45\left(\frac{D_\perp}{L}\right)^{-0.52} + 77\left(\frac{D_\perp}{L}\right)^{-1.85}. \quad (1)$$

Agreement between the results from experiments and numerical simulations is excellent. Moreover, the trend is independent of the cratering regime: identical behavior is observed in strength-dominated cratering ($S \gg 1$), gravity-dominated cratering ($S \ll 1$) and intermediate cases. As a result, this relationship is widely applicable (with the caveat that it is best supported for impact speeds less than 10 km/s) and, hence, suitable for predicting elliptical crater populations.

Table 1
Elliptical crater threshold angle as measured by laboratory experiments and numerical simulations.

Impactor diameter L (m)	Impact velocity v (km/s)	Target cohesion Y_0 (MPa)	Target friction coef. k	Gravity g (m/s^2)	Regime	Cratering efficiency $D_\perp/L$	Elliptical crater angle θ_e
1×10^{-3}	6.4	0	0.7	9.81	Gravity[a]	61.	4.75
1×10^{-3}	5	20	0	0	Strength[b]	7.0	21.
1×10^{-3}	5	200	0	0	Strength[b]	3.3	37.5
1×10^{-3}	7	200	0	0	Strength[c]	4.7	25.
1×10^{-3}	5	2	0	0	Strength[d]	11.8	13.
1×10^{-3}	5	20	0	0	strength[d]	6.4	20.
1×10^{-3}	5	200	0	0	Strength[d]	3.5	34.
1×10^{-3}	10	200	0	0	Strength[d]	5.	25.
1×10^{-3}	20	200	0	0	Strength[d]	6.5	21.
1×10^{3}	8	0	0.2	9.81	Gravity[e]	4.6	24.
1×10^{3}	8	0	0.4	9.81	Gravity[e]	4.29	26.
1×10^{3}	8	0	0.7	9.81	Gravity[e]	4.12	26.5
1×10^{3}	8	20	0.2	9.81	Intermediate[e]	3.86	28.
1×10^{3}	8	20	0.4	9.81	Intermediate[e]	3.46	30.5
1×10^{3}	8	20	0.7	9.81	Intermediate[e]	2.97	36.5
1×10^{3}	8	200	0.2	9.81	Intermediate[e]	2.3	47.
1×10^{3}	8	200	0.4	9.81	Intermediate[e]	2.16	49.5
1×10^{3}	8	200	0.7	9.81	Intermediate[e]	2.09	50.
4×10^{3}	8	0	0.2	9.81	Gravity[e]	3.75	29.5
4×10^{3}	8	0	0.4	9.81	Gravity[e]	3.6	30.
4×10^{3}	8	0	0.7	9.81	Gravity[e]	3.3	30.5
4×10^{3}	8	20	0.2	9.81	Intermediate[e]	3.03	35.
4×10^{3}	8	20	0.4	9.81	Intermediate[e]	2.88	37.
4×10^{3}	8	20	0.7	9.81	Intermediate[e]	2.65	39.
4×10^{3}	8	200	0.2	9.81	Intermediate[e]	2.05	51.
4×10^{3}	8	200	0.4	9.81	Intermediate[e]	1.99	53.
4×10^{3}	8	200	0.7	9.81	Intermediate[e]	1.89	55.

[a] Aluminum and pyrex spheres impacting quartz sand (Gault and Wedekind, 1978).
[b] Aluminum spheres into aluminum; strainless steel into lead (Burchell and Mackay, 1998).
[c] Aluminum into aluminum (Christiansen et al., 1993).
[d] Aluminum into aluminum of varying cohesion (this work and Davison et al., in press).
[e] Granite into granite of varying friction coefficient and cohesion (this work and Elbeshausen and Wünnemann, 2010).

3. Elliptical crater populations on planetary surfaces

The utility of Eq. (1) is that it can be readily combined with crater scaling laws (e.g., Holsapple, 1993) to estimate the elliptical crater threshold angle as a function of impactor and target characteristics. For example, a general scaling law for cratering efficiency in vertical impacts $D_\perp/L$ is given by:

$$\frac{D_\perp}{L} = C\left[\left(\frac{1.61gL}{v^2}\right) + \left(\frac{3.22Y}{\rho v^2}\right)^{\beta/\gamma}\right]^{-\gamma} \quad (2)$$

(Holsapple, 1993; Holsapple and Housen, 2007), where C, γ and β are constants specific to the type of target material and, here, $D_\perp$ refers to the apparent transient crater diameter, defined as the diameter of the crater as measured at the pre-impact surface, prior to any late-stage collapse that may occur. The most appropriate parameters for a planetary surface are: $C=1.29$, $\gamma=0.22$, $\beta=0.28$, $Y=1$ MPa and $\rho=3000$ kg/m^3 (Holsapple, 1993; Melosh, 1989).

Combining Eqs. (1) and (2), Fig. 2 shows the elliptical crater threshold angle as a function of gravity-scaled impact size ($1.61gL/v^2$) for three different impact velocities and the gravity regime limit ($S=0$). Also shown on Fig. 2 is the corresponding impactor diameter on Mars, assuming a constant impact velocity of 10 km/s. The

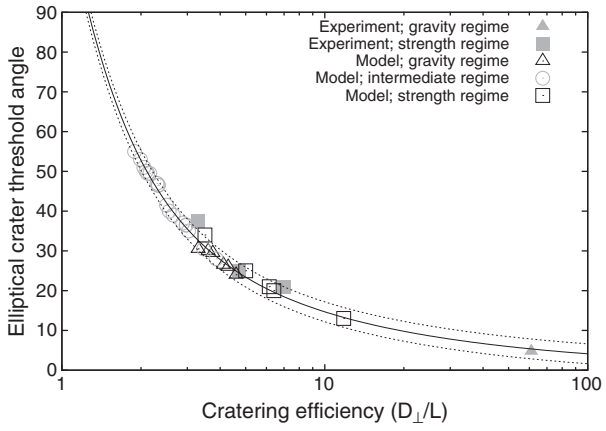

Fig. 1. Elliptical crater threshold angle θ_e as a function of the ratio of crater diameter to impactor diameter in the vertical impact case $D_\perp/L$. Also shown are the best-fit trend (Eq. (1); solid line) and this trend shifted up and down by 2.5°, the estimated maximum error in the elliptical threshold angle (dashed lines).

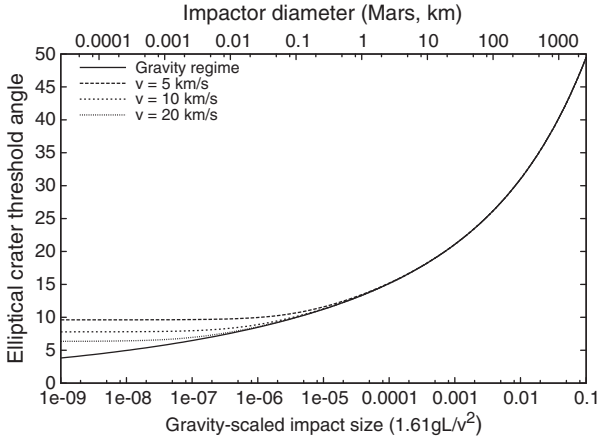

Fig. 2. Elliptical crater threshold angle θ_e as a function of gravity-scaled impact size $1.61gL/v^2$, for three different impact velocities and for the gravity regime. Upper abscissa shows the corresponding impactor diameter for impact on Mars ($g=3.71$ m/s^2; $v=10$ km/s).

decrease in cratering efficiency with increasing gravity-scaled impact size (for example, increasing impactor size at fixed velocity and gravity) implies that the elliptical crater threshold angle increases with the size of impact. For example, elliptical craters on Mars are expected to form at impact angles less than about 15° for impactors 1-km in diameter, but at angles up to 27° for impactors 100-km in diameter. Note that the present analysis does not account for planetary curvature or atmospheric shielding and so is uncertain at the extreme ends of the plot. Nevertheless, for small impacts target strength may prevent the threshold angle from becoming as low as predicted by gravity-scaling alone.

To estimate the fraction of elliptical craters as a function of size on a given planetary surface, Eq. (1) must be incorporated into a calculation of the crater size-frequency distribution (SFD) from a known impactor SFD (e.g., Ivanov, 2001, and see Appendix). We have calculated predictions of the fraction of elliptical craters as a function of crater diameter for five planetary surfaces in the inner Solar System (Fig. 3). Our model assumes an isotropic impactor flux and a Maxwellian-distribution of impact velocities (bounded by the escape velocity and an upper cutoff of 45 km/s) with a specified average impact velocity (Table 2). We used two alternative impactor SFDs: a simple power-law SFD with an exponent of −2 and a more realistic impactor SFD inferred from the actual Mars crater SFD (Ivanov, 2001; Ivanov et al., 2002). As we compute the fraction of elliptical craters for a given crater-size range, rather than the absolute number, our model does not depend on the total number of impactors, which varies depending on the planet. We restrict our analysis to impact crater diameters greater than 1 km and hence assume that transient crater size is defined by a simplified version of Eq. (2) that neglects the effect of cohesive target strength $Y=0$. Based on results of (low-velocity) laboratory and numerical impact experiments, we assume that transient crater diameter scales as the cube-root of the sine of the impact angle (Elbeshausen et al., 2009; Gault and Wedekind, 1978). Finally, we use a simple scaling law to describe the enlargement of the transient crater during complex crater collapse (McKinnon and Schenk, 1985) and assume that this modification does not alter the ellipticity of the crater.

Our model suggests that the elliptical crater populations on Earth, Mars and Venus should be very similar. Fewer elliptical craters are expected on the Moon and Mercury, primarily due to lower surface gravity and greater average impact velocity, respectively. Both these factors increase cratering efficiency, thereby reducing the elliptical crater threshold angle and making elliptical crater formation less likely. Due to the dependence of crater size on impact angle (a more oblique impact produces a smaller crater), the fraction of elliptical craters as a function of crater size is sensitive to the impactor SFD. For a power-law impactor SFD, the fraction of elliptical craters increases monotonically with crater size (gray curve, Fig. 3). In contrast, for a more realistic impactor SFD the fraction of elliptical craters is relatively constant at 2–4% for crater sizes between 5 and 100-km, before increasing rapidly at larger crater sizes (Fig. 3).

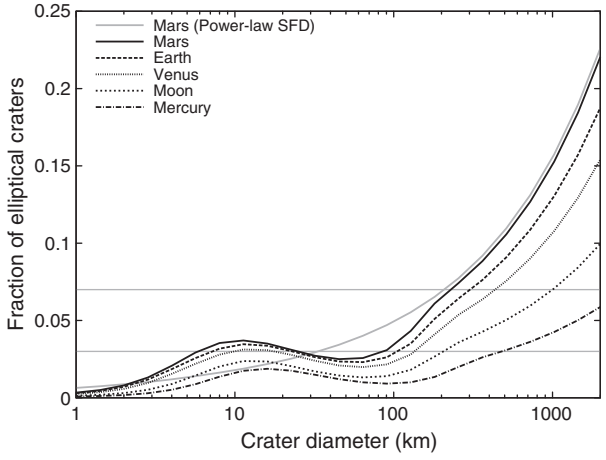

Fig. 3. Predicted fraction of fresh craters that have an ellipticity greater than 1.1 as a function of crater diameter. Black lines show the fractional elliptical crater SFD for the five major planetary surfaces in the inner Solar System assuming a common impactor SFD inferred from the Mars crater SFD (Ivanov et al., 2002). The thick gray curve shows the equivalent fractional elliptical crater SFD for Earth assuming a power-law impactor SFD with exponent −2. The thin gray horizontal lines show the 5 ± 2% bounds on the number of elliptical craters on the Moon, Mars and Venus, established from observational studies (Bottke et al., 2000; Schultz and Lutz-Garihan, 1982).

Table 2
Model parameters for elliptical crater SFD calculation.

Planetary surface	Surface gravity (m/s^2)	Escape velocity (km/s)	Average impact velocity[a] (km/s)	Simple-to-complex diameter[b] (km)
Earth	9.81	11.2	17.2	4
Mars	3.71	5.	9.6[c]	7
Venus	8.87	10.6	19.2	4[d]
Mercury	3.7	4.25	30.	10
Moon	1.63	2.4	13.	20

[a] Bottke et al. (1994).
[b] Melosh (1989).
[c] Ivanov (2001).
[d] Assumed equivalent to Earth.

Our model does not consider the effect of planetary curvature or atmospheric interaction on elliptical crater formation. For planets with an atmosphere, small impactors will decelerate during atmospheric traverse and their trajectory to the target plane will steepen. In this case, calculating the probability of elliptical crater formation is non-trivial. The size of the largest impactor significantly affected by atmospheric interaction depends on impactor composition, density of the atmosphere and surface gravity. We estimate (very approximately) that this applies to impactors as large as 70 m (corresponding crater size is 1.5 km) on Earth, 1 m (50 m) on Mars and 5 km (35 km) on Venus. At the other end of the crater-size spectrum, crater ellipticity may be affected as impactor radius becomes a significant fraction of the radius of the target planet (Andrews-Hanna and Zuber, 2010; Marinova et al., 2008, 2011), so long as it is small enough not to cause catastrophic disruption. Applying a simple geometric model, Andrews-Hanna and Zuber (2010) suggested that planetary curvature is likely to increase crater ellipticity significantly, relative to the estimates presented here that assume a flat surface, for craters larger than ~500-km diameter on Mars and ~250-km diameter on the Moon. However, recent SPH calculations of giant impacts suggest that planetary curvature may have little influence on crater ellipticity, particularly when impact velocity is greater than a few km/s (Marinova et al., 2011).

4. Comparison with observations

Our model predictions are consistent with observations that show 5 ± 2% of impact craters (in the 5–100-km diameter size range) on the Moon, Mars and Venus are elliptical ($e>1.1-1.2$; Bottke et al., 2000; Schultz and Lutz-Garihan, 1982). Those studies found no dependence on crater size, which is also consistent with our model for the 5–100-km diameter size range (Fig. 3). Our model predicts a slightly lower fraction of elliptical craters on the Moon relative to Mars and Venus, although the difference is likely to be hard to detect from observations given the small numbers of elliptical craters. Elliptical crater statistics from Mercury may offer a better test of the model, particularly as new data from the MESSENGER spacecraft becomes available.

The best database for detailed testing of our model is Mars. Thorough examinations of elliptical craters on Mars were conducted by Schultz and Lutz-Garihan (1982) and Bottke et al. (2000) using Viking images. Schultz and Lutz-Garihan (1982) measured martian

craters larger than 5 km, on several young terrains, for high ellipticity ($e > 1.1$), butterfly-wing ejecta patterns, and other features diagnostic of oblique impact (Gault and Wedekind, 1978). They concluded that overall about $5 \pm 2\%$ of craters were elliptical (and caused by oblique impact). A similar result was obtained by Bottke et al. (2000), who reexamined the elliptical crater dataset used by Schultz and Lutz-Garihan (1982) and an independent elliptical crater survey ($e \geq 1.2$; Barlow, 1988). To minimize the effect of post-impact modification (e.g., erosion and tectonism) on crater shape many elliptical craters from both datasets were excluded. Nevertheless, estimates of the fraction of elliptical craters on specific units agreed to within 0.5–1%.

To supplement and extend previous studies we compiled a new elliptical crater database (Table 3; Robbins and Hynek, 2010; Robbins, 2011) using THEMIS data (Christensen et al., 2003) and MOLA topography data (Smith et al., 2001). In ArcGIS, craters were visually identified in THEMIS Daytime IR planetary mosaics over-sampled to a scale of ~1:250,000 on-screen. Crater rims were outlined using ArcGIS's "streaming" tool by laying down one vertex every 500 m. The combination of over-sampling visually (viewing one pixel on the map as more than one pixel on the screen) and under-sampling in outlining (creating one vertex for every ~5 pixels as opposed to every pixel) helped to reduce errors in outlining rims and reduce the time necessary for this task due to a decreased need for higher precision manual dexterity. Vertices were recorded in decimal degrees. The polygons representing each crater rim were then imported into Igor Pro software where we used a non-linear least-squares (NLLS) fitting algorithm to a circle to determine the center latitude and longitude of each crater as well as its diameter and a similar NLLS ellipse-fit to determine major and minor axes, tilt, and center latitude and longitude. The NLLS algorithm accounts for map projection by converting the decimal degrees into meters from the polygon's centroid, accounting for the first-order spherical surface of Mars. This is a minor correction for craters on the kilometer scale near the equator, but it is a necessary correction for larger craters and craters at latitudes larger than ~±30°.

After crater rims were analyzed and diameters calculated, standard crater size-frequency distributions (SFDs) were created. These were done by binning in multiplicative $D\sqrt{2}$ intervals and center-weighting the bins based on the local SFD slope. Uncertainties were calculated as $\pm\sqrt{N}$ where N is the number of craters in each bin, following the Crater Analysis Techniques Working Group (1979). The elliptical crater SFD was then normalized based on the total number of craters in each bin from the global Mars catalog (Robbins, 2011).

A four-point classification system was used to categorize each crater's degradation/modification state, where "1" was considered highly degraded and "4" morphologically pristine. The classification system, which is described in detail in Robbins (2011), is a simplification of the system proposed by Barlow (2004). Craters were manually examined and the preservation state of the rim, floor, and ejecta were assessed by eye, and the depth/diameter ratio relative to a fresh crater of that diameter was calculated. These characteristics were combined to give the final 1–4 classes. Fig. 4A shows an example of a Class 3 crater with partially buried ejecta and minor floor deposits, while Fig. 4B shows a Class 4 crater with no obvious floor deposits, only two minor impacts on its ejecta, and a pristine rim. In the work presented here, a "fresh" crater is a crater with a classification of 3 or 4, while an "undegraded" crater is a crater with a classification of 2 or higher.

Fig. 4 shows three example craters from the database that are similar in size (~20-km diameter) but differ in ellipticity. A proportion of elliptical craters display clear evidence of oblique impact, such as a characteristic butterfly ejecta pattern (Fig. 4B), with a line of

Table 3
Elliptical craters on Mars.

All craters[a]			Undegraded craters[b]		Fresh craters[c]	
Crater diameter (km)	Total number of craters	Number of elliptical craters	Total number of craters	Number of elliptical craters	Total number of craters	Number of elliptical craters
9.39	77838	4904	4698	177	2963	60
13.2	6033	398	3007	124	1786	41
18.7	4683	304	2168	77	1185	21
26.2	3420	235	1436	63	645	6
36.8	2216	144	968	29	331	4
51.5	1295	60	580	16	142	2
71.8	583	35	277	12		
101.	221	10	104	2		
142.	68	8	19	5		
204.	29	3				
289.	17	5				

[a] Craters of all degradation states (classes 1–4).
[b] All but the most heavily degraded craters (classes 2–4).
[c] Only fresh craters with (near) pristine morphology (classes 3 and 4). See text and Robbins (2011) for more details.

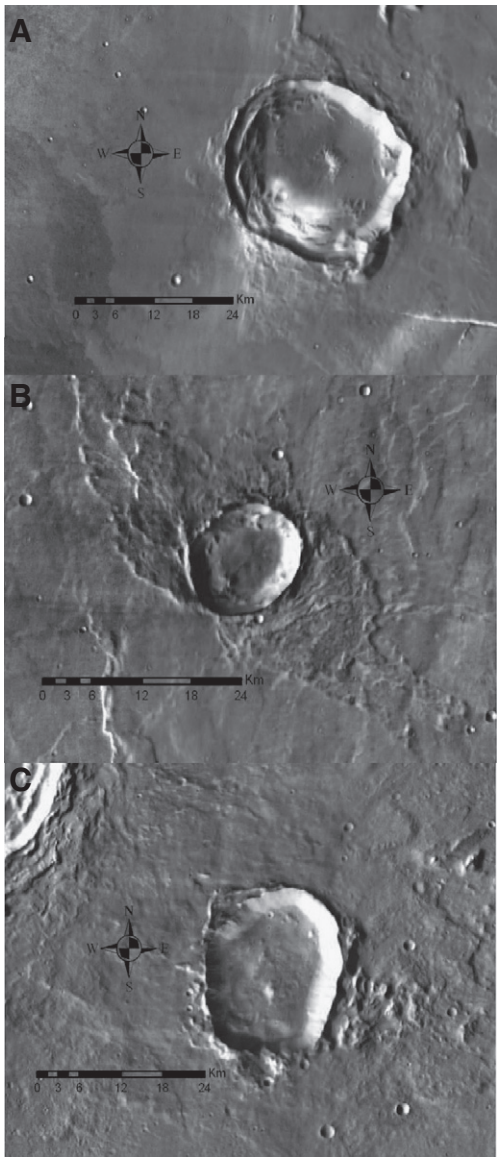

Fig. 4. THEMIS images of example craters on Mars of similar size (~20-km diameter) and varying ellipticity. (A) Near-circular crater (e = 1.05). (B) Elliptical crater (e = 1.2) with obvious butterfly ejecta pattern symmetric about the long-axis of the crater. In this case, ellipticity is very likely due to oblique impact. (C) Elliptical crater (e = 1.25) with less obvious ejecta. In this case, ellipticity may be due to oblique impact or some other process, such as binary impact. Images taken from THEMIS Daytime IR mosaics at 100 mpp (Christensen et al., 2010).

symmetry parallel to the long-axis of the elliptical crater (Gault and Wedekind, 1978). In such cases, crater ellipticity is almost certainly due to oblique impact. However, many other elliptical craters in the database do not show (obvious) independent evidence of oblique impact (Fig. 4C). In this case, crater ellipticity might be due to another mechanism, such as closely-separated binary impact or post-impact modification. Due to the large number of elliptical craters it was not possible to examine each one for additional indicators of oblique impact or signs of post-impact modification. To reduce the influence of post-impact modification, the more conservative ellipticity threshold of $e>1.2$ (Bottke et al., 2000) was used to define an elliptical crater.

Fig. 5 compares the modeled fraction of elliptical craters as a function of crater diameter with the observed population of elliptical craters on Mars. Elliptical crater numbers (Table 3) are plotted for all degradation states (all, triangles), for all but the most-degraded craters (undegraded, squares) and for only pristine craters (fresh, circles). The three different crater populations show the same qualitative trend of a constant fraction of elliptical craters for diameters between 5 and 100 km. In general, the new observational data plot within the range of previous estimates for the fraction of elliptical craters on Mars (shown as gray horizontal lines). There is, however, a systematic increase in the percentage of elliptical craters with increasing degradation of morphology: 1.9% of fresh craters (degradation class 3 and 4) larger than 8.5 km have an ellipticity greater than 1.2, while the percentage of elliptical craters of the same size rises to 3.8% for undegraded craters (class 2–4) and 6.3% for all craters, including those most degraded (class 1). The reason for this trend is unclear but is likely due, at least in part, to an increased uncertainty in ellipse-fitting for highly-degraded craters where a large section of the crater rim is missing. A non-trivial fraction of the craters determined to be degraded and elliptical have a poorly defined rim where less than 50% is visible. Because there are five free parameters in the best-fit ellipse, it is significantly more likely for the fitting algorithm to select a more elliptical best-fit ellipse for the crater when presented with a partial rim outline as opposed to a near complete rim outline. In addition, in situations where the rim is degraded it is more likely that a feature identified as a single crater could actually be two superimposed or doublet craters but with the tell-tale cusps of overlapping rims completely eroded away. On the other hand, as it is unlikely that erosion or tectonism would systematically increase crater ellipticity, the elliptical crater statistics in the total crater population, which includes over ten times more craters than the fresh population, may well reflect a robust trend.

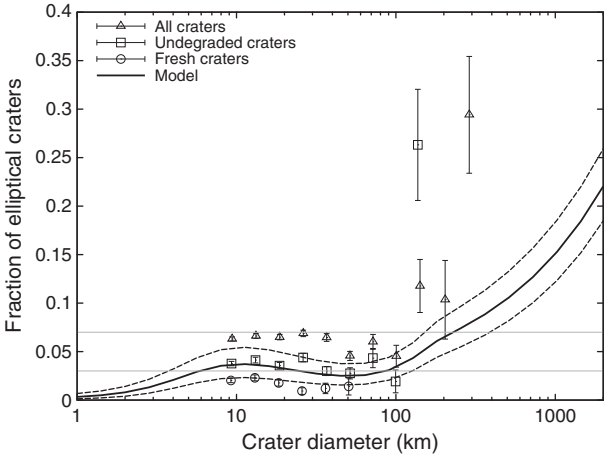

Fig. 5. Fraction of elliptical Martian craters as a function of crater diameter. Solid black line shows the model prediction for Mars using the elliptical threshold angle trend defined by Eq. (1). Dashed black lines above and below the solid line show the sensitivity of the model to a $\pm 2.5°$ uncertainty in the threshold angle. Points show elliptical craters on Mars, identified using THEMIS and MOLA data, for crater populations of different degradation states (see Table 3). The crater SFDs were binned in multiplicative $D\sqrt{2}$ intervals; uncertainties were calculated as $\pm\sqrt{N}$ where N is the number of craters in each bin. The elliptical crater SFD was then normalized based on the total number of craters in each bin from the global Mars catalog (Robbins, 2011). Gray horizontal lines show the $5\pm 2\%$ bounds on the number of fresh elliptical craters established from previous observational studies (Bottke et al., 2000; Schultz and Lutz-Garihan, 1982).

For impact crater diameters between 5 and 100 km the model prediction and the new observational data are in qualitative agreement, both showing that the fraction of elliptical craters is constant (or decreases slightly) with increasing crater size. The predicted elliptical crater SFD (craters with ellipticity greater than 1.1; solid line) agrees well with the observed fraction of undegraded craters with ellipticity greater than 1.2. The dashed lines in Fig. 5 illustrate the sensitivity of our predicted elliptical crater SFD to one uncertainty in the model: the elliptical crater threshold angle, as defined by Eq. (1). The minimum bound for our predicted population, illustrated by the lower dashed line, which assumes an elliptical crater threshold angle 2.5° lower than Eq. (1), is in good agreement with the observed fraction of fresh craters with ellipticity greater than 1.2. This is consistent with the results of numerical models and laboratory experiments, which show that the impact angle required to form a crater with an ellipticity of 1.2 is a few degrees below that required to form a crater with an ellipticity of 1.1 (e.g., Burchell and Mackay, 1998; Davison et al., in press). The maximum bound for our predicted population, illustrated by the upper dashed line, which assumes an elliptical crater threshold angle 2.5° greater than Eq. (1), is close to but below the new observational data for craters of all degradation states. If this dataset is an accurate representation of the total proportion of elliptical craters on Mars it is likely that this population also includes elliptical craters formed by a mechanism other than oblique impact (i.e., not included in our model), such as impact of a highly-elongated single asteroid or a closely-separated binary asteroid.

Both the model and observations (for all craters) suggest that the fraction of elliptical impact craters is much greater among the large basins than among small craters. For impact crater diameters greater than 100 km the model results and observational data show a significant increase in the fraction of elliptical craters as a function of crater size, although the rate of increase in the observational data is more dramatic. The discrepancy between model and observation at these larger crater sizes might be due in part to small number statistics (the largest two crater size bins for the "all craters" population include only 8 elliptical craters, see Table 3). However, the size of the discrepancy suggests that there may be an additional source of elliptical craters. Alternatively, it may suggest that one (or more) of our model assumptions is incorrect at large sizes. In particular, the assumed impactor SFD may be inappropriate or crater collapse may actually enhance, rather than simply preserve, crater ellipticity. Large-scale target heterogeneity, such as variations in crustal thickness, may also enhance the ellipticity of large craters. For craters larger than 500-km in diameter the curvature of Mars may also influence crater ellipticity (Andrews-Hanna and Zuber, 2010); however, the effect of target curvature on crater ellipticity is not fully understood (Marinova et al., 2011). Future work will quantitatively examine these hypotheses.

5. Discussion

Our analysis of 3D numerical impact simulations and laboratory experiments demonstrates that the threshold impact angle below which an elliptical ($e>1.1$) crater is formed is a function of cratering efficiency, regardless of the target material or cratering regime. A simple, intuitive geometric rationale for this relationship was discussed by Bottke et al. (2000) based on the impact-explosion analogy (Gifford, 1924, 1931; Ives, 1919). Numerical simulations permit further insight into this relationship. In an oblique impact the nascent crater exhibits a maximum ellipticity a short time after the projectile contacts the target

surface, although (based on our numerical simulations) this never approaches the projection of the impactor onto the target plane (i.e., $L/(L \sin\theta)$). At this early stage of crater growth the inertial stresses are so high that the influences of gravity and strength are insignificant and so do not affect crater ellipticity. As the crater expands the planform progressively loses its asymmetry and the effects of gravity (the weight of the displaced mass) and strength begin to arrest crater growth. The greater the weight of the displaced mass and/or the strength of the target, the earlier crater growth is ceased and, consequently, the more elliptical the final crater. For the same reason, other features indicative of oblique impact are also likely to be more evident in large impact craters (Schultz, 1992).

Using the results of our analysis, we have calculated the expected fraction of elliptical craters as a function of crater size for the terrestrial planets and compared our predictions with new observational data from Mars. Our results suggest that for crater diameters between 5 and 100 km, 2–4% of craters in a fresh impact crater population on the terrestrial planets are expected to be elliptical, consistent with the lower bound of previous estimates (Bottke et al., 2000; Schultz and Lutz-Garihan, 1982). A new database of Martian craters derived from THEMIS and MOLA data (Robbins, 2011; Robbins and Hynek, 2010) suggests that 2% of fresh craters and 6% of all craters in this size range are elliptical. It is possible that the larger fraction of elliptical craters observed in the total population, relative to the fresh population and that predicted by our model, is due to uncertainty in measuring the ellipticity of heavily degraded craters. On the other hand, the discrepancy may suggest that the total crater population includes elliptical craters formed by both oblique impact and an additional mechanism, such as impact of a highly elongated single asteroid or closely separated binary. Minor differences in elliptical crater populations between planets are expected, but may be hard to detect. For craters larger than 100 km in diameter, the predicted fraction of elliptical craters rises dramatically with crater size. This prediction is supported by the observed elliptical craters on Mars. As large impact basins are more likely to be elliptical than small and medium size craters, they offer the best natural laboratory for oblique impact processes.

Acknowledgments

This work was funded by NERC grant NE/E013589/1, DFG grant WU 355/5-2 and the Helmholtz-Alliance HA-203. We are grateful to Boris Ivanov and an anonymous reviewer for very helpful reviews that improved this manuscript.

Appendix A. Elliptical Crater SFD calculation

Ivanov (2001) describes how to compute the size-frequency (diameter-number) distribution (SFD) of impact craters $N(>D)$ on a planetary surface from a known size-frequency (diameter-number) distribution of impactors $N(>L)$. Central to this calculation is the relationship:

$$\frac{dN}{dD} = \int_{vmin}^{v_{max}} \int_{\theta_{min}}^{\theta_{max}} \left[\frac{dN}{dL}\frac{dL}{dD}\right] f_v(v) f_\theta(\theta) d\theta\, dv. \quad (A.1)$$

In this equation, dN/dL is the slope of the impactor SFD, dL/dD is the derivative of impactor diameter with respect to crater diameter, $f_v(v)\,dv$ is the probability of an impact of velocity between v and $v+dv$ and $f_\theta(\theta)d\theta$ is the probability of impact at an angle (to the target plane) between θ and $\theta+d\theta$. In this work, we solve this equation numerically to calculate the SFD of elliptical craters (for which $\theta_{min}=0$, $\theta_{max}=\theta_e$), as well as the SFD for all craters, and use these to determine the fraction of elliptical craters as a function of crater size. The steps and assumptions in our approach are described below; for clarity, a Python-script implementation of our algorithm is included in Supporting Material.

Our general approach for solving Eq. (A.1) is to consider a single crater size bin, of representative size D, and numerically evaluate the double integral over impact velocity and angle to give dN/dD. However, straightforward numerical integration of the double integral is complicated by the fact that the relationship between impactor size and final crater size (dL/dD) is different for small, simple craters, which do not undergo substantial late-stage gravitational collapse, and for large, complex craters, which do. To account for this, we first define a set of final rim-to-rim crater diameter bins, with intervals starting at $D_f=1$ km and increasing by a factor of $\sqrt{2}$, within which we wish to know the fraction of elliptical craters. We then convert these final rim-to-rim crater diameter bin intervals D_f into their corresponding apparent transient crater diameter bin intervals D (that is, the diameter of the pre-collapse crater as measured at the pre-impact surface) using observational crater scaling relationships for simple and complex craters:

$$D_f = 1.17 max\left(D, \frac{D^{1.13}}{D_{sc}^{0.13}}\right), \quad (A.2)$$

where D_{sc} is the simple-to-complex transition diameter on the target surface (Collins et al., 2005; McKinnon and Schenk, 1985). In adopting this approach, we assume that the ellipticity of the final crater is the same as that of the transient crater.

In addition, we subdivide each transient crater size bin into many sub-bins, with intervals spaced in a geometric progression. For each sub-bin, we evaluate the double integral in Eq. (A.1) assuming a constant, representative value of the transient crater diameter in the bin D (the geometric mean of the left and right bin interval). We then sum the results from each sub-bin to arrive at the number of elliptical craters N_e, the total number of craters N and the fraction of elliptical craters f_e in the original, rim-to-rim, final crater diameter bin. For example, the fraction of elliptical craters f_e with transient crater diameters between D_l and D_u can be computed by evaluating the integral:

$$f_e(D_l, D_u) = \int_{D_l}^{D_u} \frac{dN_e/dD}{dN/dD} dD. \quad (A.3)$$

The outer numerical integral in Eq. (A.1) sums over impact velocity. We approximate the probability of an impact of velocity between v and $v+dv$ by a Maxwellian distribution:

$$f_v(v)dv = \sqrt{\frac{2}{\pi}}\frac{(v-v_{esc})^2}{a^3} exp\left(-\frac{(v-v_{esc})^2}{2a^2}\right) dv, \quad (A.4)$$

where v_{esc} is escape velocity and a is related to the average impact velocity, v_{av}, by $a=\sqrt{\pi/8}(v_{av}-v_{esc})$. Table 2 lists the average impact velocity and escape velocity for each planetary surface considered here. The minimum velocity in the integration is the escape velocity; the maximum velocity depends upon the orbital parameters of the impactor population and the target planet, but here we assume a constant upper limit of 45 km/s.

The inner integral sums over impact angle. The probability of an impact angle (to the target plane) between θ and $\theta+d\theta$ for an isotropic impactor population striking a spherical, airless, gravitating planet is given by (Shoemaker, 1962)

$$f_\theta(\theta)d\theta = 2 \sin\theta \cos\theta\, d\theta. \quad (A.5)$$

For the total impact crater population $N(>D)$, the integral limits on impact angle are $0<\theta<\pi/2$. For the elliptical crater population ($N_e(>D)$; all craters with ellipticity greater than 1.1), the limits are $0<\theta<\theta_e$, where θ_e is the elliptical crater threshold angle, which is assumed to be constant in each sub-bin for a given impact velocity. We estimate θ_e using Eq. (1), where $D_\perp/L$ is the vertical impact cratering efficiency for the transient

crater diameter D. We note that, in reality, some craters in a single sub-bin will be formed by oblique impact of a larger projectile, whereas others will be formed by a steep impact of a smaller projectile. In each case, the vertical-impact cratering efficiency will be slightly different (because the projectile size differs), implying that the elliptical threshold angles will differ. However, we have verified by Monte-Carlo simulation that for small enough transient crater size bins (i.e., by dividing the main transient crater size bin into sufficiently many sub-bins) the error in the number of elliptical craters is very small, and our approach is valid.

The derivative dL/dD in Eq. (A.1) can be estimated using an empirical scaling law that relates transient crater diameter to the impactor diameter L, surface gravity g, impact velocity and impact angle (e.g., Eq. (2); Holsapple, 1993). Neglecting the effect of cohesive target strength at very small crater diameters ($Y=0$) and rearranging Eq. (2) as appropriate for rocky planetary surfaces, gives

$$D_{\perp} = 1.161 g^{-0.22} v^{0.44} L^{0.78}. \tag{A.6}$$

To account for the effect of impact angle on transient crater size, we assume that transient crater volume scales linearly with the sine of the impact angle, as suggested by low-velocity laboratory experiments and numerical simulations of oblique impacts (Elbeshausen et al., 2009; Gault and Wedekind, 1978). This assumption leads to

$$D = D_{\perp} sin^{1/3}\theta = 1.161 g^{-0.22} v^{0.44} L^{0.78} sin^{1/3}\theta. \tag{A.7}$$

Rearranging Eq. (A.7) gives:

$$L = 0.825 g^{0.282} v^{-0.564} D^{1.282} sin^{-0.42}\theta \tag{A.8}$$

which can easily be differentiated to give:

$$\frac{dL}{dD} = 1.06 g^{0.282} v^{-0.564} D^{0.282} sin^{-0.42}\theta. \tag{A.9}$$

For a simple power-law impactor SFD, $N(>L) = cL^{-b}$, the derivative dN/dL in Eq. (A.1) is given by

$$\frac{dN}{dL} = -bcL^{-(b+1)}, \tag{A.10}$$

which can be readily evaluated as a function of D by substituting Eq. (A.8). A more accurate model of the impactor SFD for the inner Solar System was defined by Ivanov et al. (2002) using a relative SFD $R(>L)$ described by a 15th-order polynomial function of L (for $L<27$ km). We use this SFD, together with the identity $dN/dL \equiv R(>L)/L^3$ and Eq. (A.8) to calculate dN/dL as a function of D. For $L>27$ km we assume a smooth extrapolation of the SFD with a constant exponent of -2.

References

Amsden, A.A., Ruppel, H.M., 1981. SALE-3D: a simplified ALE computer program for calculating three-dimensional fluid flow. LA-8905, Los Alamos National Laboratory, Los Alamos, NM, undefined Los Alamos National Laboratory Report SALE-3D: A simplified ALE computer program for calculating three-dimensional fluid flow.

Anderson, J.L.B., Schultz, P.H., Heineck, J.T., 2004. Experimental ejection angles for oblique impacts: implications for the subsurface flow-field. Meteorit. Planet. Sci. 39 (2), 303–320.

Andrews-Hanna, J.C., Zuber, M.T., 2010. Elliptical craters and basins on the terrestrial planets. In: Large Meteorite Impacts and Planetary Evolution, vol. IV. Geological Society of America Special Papers, GSA, Boulder, CO, 465, pp. 1–13. doi:10.1130/2010.2465(01).

Barlow, N.G., 1988. Crater size-frequency distributions and a revised martian relative chronology. Icarus 75 (2), 285–305.

Barlow, N.G., 2004. Martian subsurface volatile concentrations as a function of time: clues from layered ejecta craters. Geophys. Res. Lett. 31 (5).

Bottke, W.F., Nolan, M.C., Greenberg, R., Kolvoord, R.A., 1994. Collisional lifetimes and impact statistics of Near-Earth asteroids. In: Gehrels, T. (Ed.), Hazards Due to Comets and Asteroids. University of Arizona Press, Tucson, pp. 337–357.

Bottke, W.F., Love, S.G., Tytell, D., Glotch, T., 2000. Interpreting the elliptical crater populations on mars, venus, and the moon. Icarus 145 (1), 108–121.

Burchell, M.J., Mackay, N.G., 1998. Crater ellipticity in hypervelocity impacts on metals. J. Geophys. Res. 103 (E10), 22761–22774.

Christensen, P.R., Bandfield, J.L., III, J.F.B., Gorelick, N., Hamilton, V.E., Ivanov, A., Jakosky, B.M., Kieffer, H.H., Lane, M.D., Malin, M.C., McConnochie, T., McEwen, A.S., McSween, H.Y., Mehall, G.L., Moersch, J.E., Nealson, K.H., Rice, J.W., Richardson, M.I., Ruff, S.W., Smith, M.D., Titus, T.N., Wyatt, M.B., 2003. Morphology and composition of the surface of mars: Mars odyssey THEMIS results. Science 300 (5628), 2056–2061.

Christensen, P.R., Gorelick, N., Mehall, G.L., Murray, K., 2010. THEMIS public data releases, planetary data system node. URL http://themis-data.asu.edu.

Christiansen, E.L., Cykowski, E., Ortega, J., 1993. Highly oblique impacts into thick and thin targets. Int. J. Impact Eng. 14, 157–168.

Collins, G.S., Melosh, H.J., Marcus, R.A., 2005. Earth impact effects program: a web-based computer program for calculating the regional environmental consequences of a meteoroid impact on earth. Meteorit. Planet. Sci. 40 (6), 817–840.

Crater Analysis Techniques Working Group, 1979. Standard techniques for presentation and analysis of crater size-frequency data. Icarus 37 (2), 467–474.

Davison, T.M., Collins, G.S., Elbeshausen, D., Wünnemann, K., Kearsley, A., in press. Numerical modeling of oblique hypervelocity impacts on high strength ductile targets. Meteoritics & Planetary Science.

Elbeshausen, D., Wünnemann, K., 2010. The transition from circular to elliptical impact craters. EPSC Abstracts, Abstract EPSC2010-73, vol. 5. Copernicus, European Planetary Science Congress 2010, Rome.

Elbeshausen, D., Wünnemann, K., Collins, G.S., 2009. Scaling of oblique impacts in frictional targets: implications for crater size and formation mechanisms. Icarus 204 (2), 716–731.

French, B., Koeberl, C., 2010. The convincing identification of terrestrial meteorite impact structures: what works, what doesn't, and why. Earth Sci. Rev. 98 (1–2) 170, 123.

Gault, D.E., Wedekind, J., 1978. Experimental studies of oblique impact. Proc. Lunar and Planet. Sci. Conf. 9th, pp. 3843–3875.

Gifford, A., 1924. The mountains of the moon. N.Z. J. Sci. Technol. 7, 129.

Gifford, A.C., 1931. The origin of the surface features of the moon. J. R. Astron. Soc. Can. 25, 70.

Gilbert, G.K., 1893. The moon's face: a study of the origin of its features. Bull. Phil. Soc. Wash. 12, 241–292.

Herrick, R.R., Forsberg-Taylor, N.K., 2003. The shape and appearance of craters formed by oblique impact on the moon and venus. Meteorit. Planet. Sci. 38, 1551–1578.

Holsapple, K.A., 1993. The scaling of impact processes in planetary sciences. Annu. Rev. Earth Planet. Sci. 21, 333–373.

Holsapple, K.A., Housen, K.R., 2007. A crater and its ejecta: an interpretation of deep impact. Icarus 187 (1), 345–356.

Holsapple, K.A., Schmidt, R.M., 1979. A material-strength model for apparent crater volume. Proceedings Lunar and Planetary Science Conference 10th, vol. 3. Pergamon Press, New York.

Ivanov, B.A., 2001. Mars/Moon cratering rate ratio estimates. Space Sci. Rev. 96 (1), 87.

Ivanov, B.A., Neukum, G., Bottke, W.F., Hartmann, W.K., 2002. The comparison of size-frequency distributions of impact craters and asteroids and the planetary cratering rate. Asteroids III. University of Arizona Press, Tucson, pp. 89–101.

Ives, H.E., 1919. Some large-scale experiments imitating the craters of the moon. Astrophys. J. 50, 245.

Marinova, M.M., Aharonson, O., Asphaug, E., 2008. Mega-impact formation of the mars hemispheric dichotomy. Nature 453 (7199), 1216–1219.

Marinova, M.M., Aharonson, O., Asphaug, E., 2011. Geophysical consequences of planetary-scale impacts into a mars-like planet. Icarus 211 (2), 960–985 Feb.

McKinnon, W.B., Schenk, P.M., 1985. Ejecta blanket scaling on the Moon and Mercury — inferences for projectile populations. Lunar and Planet. Sci. Conf. Proceedings XVI. Lunar and Planetary Institute, Houston, Texas, pp. 544–545.

Melosh, H.J., 1977. Crater modification by gravity: a mechanical analysis of slumping. In: Roddy, D.J., Pepin, R.O., Merrill, R.B. (Eds.), Impact and explosion cratering. Pergamon Press, New York, pp. 1245–1260.

Melosh, H.J., 1989. Impact Cratering: A Geological Process. Oxford University Press.

Robbins, S., 2011. Planetary surface properties, cratering physics, and the volcanic history of mars from a new global martian crater database. Ph.D. thesis, University of Colorado at Boulder.

Robbins, S., Hynek, B., 2010. Progress torwards a new global catalog of martian craters and layered ejecta properties, complete to 1.5 km. 41st Lunar and Planetary Science Conference. Lunar and Planetary Institute, Houston, TX. Abstract #2257.

Schultz, P.H., 1992. Atmospheric effects on ejecta emplacement and crater formation on venus from magellan. J. Geophys. Res. 97 (E10) 16,183–16,248.

Schultz, P.H., Lutz-Garihan, A.B., 1982. Grazing impacts on mars — a record of lost satellites. J. Geophys. Res. 87, A84–A96.

Shoemaker, E.M., 1962. Interpretation of lunar craters. In: Kopal, A. (Ed.), Physics and astronomy of the Moon. Academic Press, New York, pp. 283–351.

Smith, D.E., Zuber, M.T., Frey, H.V., Garvin, J.B., Head, J.W., Muhleman, D.O., Pettengill, G.H., Phillips, R.J., Solomon, S.C., Zwally, H.J., Banerdt, W.B., Duxbury, T.C., Golombek, M.P., Lemoine, F.G., Neumann, G.A., Rowlands, D.D., Aharonson, O., Ford, P.G., Ivanov, A.B., Johnson, C.L., McGovern, P.J., Abshire, J.B., Afzal, R.S., Sun, X., 2001. Mars orbiter laser altimeter: experiment summary after the first year of global mapping of mars. J. Geophys. Res. 106 (E10) 23,689–23,722.